Photoelectrocatalytic Green Hydrogen Production from Coconut Water Waste Using Carbon-MgO Nanocomposite-Modified Electrodes

Abdul Haris Watoni [a,1,*], Aisyah Rahmawati [a,2], La Ode Ahmad Nur Ramadhan [a,3], Thamrin Azis [a,4], Fahmiati [a,5], La Ode Kadidae [a,6], Laode Abdul Kadir [a,7]

[a] Department of Chemistry, Mathematics and Natural Sciences, Universitas Halu Oleo, Kendari, Indonesia
[1] ahwatoni@gmail.com*; [2] aisyahrahmawati13005@gmail.com; [3] ramadhan305@gmail.com; [4] thamrinazis06@gmail.com; [5] fahmiati@uho.ac.id; [6] laode.kadidae@uho.ac.id; [7] kadir20512048@gmail.com
* corresponding author

ARTICLE INFO

Article history
Received May 19, 2026
Revised August 27, 2026
Accepted August 27, 2026

Keywords
C–MgO
Green hydrogen
Photoelectrocatalysis
Red dragon peel extract

ABSTRACT

Hydrogen is considered a promising alternative to fossil fuels; however, conventional water electrolysis requires substantial energy input and may have limited environmental efficiency. This study investigates the synthesis of carbon–magnesium oxide (C–MgO) nanocomposites mediated by red dragon fruit (Hylocereus polyrhizus) peel extract to enhance green hydrogen production from coconut water waste via photoelectrocatalysis. The nanocomposite was synthesized using a hydrothermal method and characterized using UV–Vis spectroscopy, Fourier-transform infrared spectroscopy (FTIR), and X-ray diffraction (XRD). UV–Vis analysis indicated good optical stability, with a main absorption band at 400–500 nm and a band gap energy of 2.48–2.66 eV, indicating suitability for visible-light-driven photoelectrocatalysis. FTIR analysis confirmed the presence of –OH, C=C, C=O, and Mg–O functional groups. XRD results revealed the characteristic diffraction pattern of C–MgO with a cubic crystal structure and an average crystallite size of 17.41 nm. These physicochemical properties contributed to improved photoelectrocatalytic hydrogen production. Conventional electrolysis of coconut water produced hydrogen at a rate of 0.3636 mL/min, whereas photoelectrocatalysis using a C–MgO 1:3-modified electrode achieved a production rate of 3.1489 mL/min. The incorporation of carbon and MgO into the electrode modifier increased the hydrogen production rate by 766.03% compared with conventional electrolysis. Overall, the results demonstrate that the biosynthesized C–MgO nanocomposite effectively enhances visible-light-driven photoelectrocatalytic hydrogen production from coconut water waste, offering a promising approach for waste valorization and sustainable green hydrogen generation.

1. Introduction

Global dependence on fossil fuels continues to increase, alongside rapid population growth and industrialization. In addition to causing an energy crisis, the continued use of fossil fuels is also a major contributor to increasing greenhouse gas emissions. As awareness of the negative impacts of fossil fuel use grows, various countries are turning to sustainable alternative energy sources. One energy source considered to have significant potential is green hydrogen. The combustion process of hydrogen gas is highly exothermic and carbon-free, as water (H_2O) is the sole product [1]. In addition, hydrogen gas can release combustion heat of up to 141 MJ/kg, much higher than the combustion heat of fossil fuels such as gasoline (48 MJ/kg), LPG (49.80 MJ/kg), diesel (44.80 MJ/kg), charcoal (32.50

mJ/kg), kerosene (42.20 MJ/kg), even wood (21.70 MJ/kg) [2]. The same source report also indicates that hydrogen is more flammable than all fossil fuels, with a minimum ignition energy of 0.017 mJ.

Green hydrogen can be produced through water electrolysis. However, the availability of fresh water is limited, so switching to wastewater instead of fresh water is the key solution to this problem. Producing hydrogen from wastewater turns toxic liquid waste and sewage into clean energy. It solves a dual crisis by replacing the high volumes of pure fresh water normally needed for green hydrogen electrolysis while simultaneously cleaning the water [3]. Utilizing coconut water waste as an alternative energy source can also reduce environmental pollution [4]. Coconut water contains 95.5% water, 0.1% fat, 4% carbohydrates, 0.02% calcium, 0.01% phosphorus, 0.5% iron, and several amino acids, vitamin B complex, vitamin C, and mineral salts [5]. Due to its high water content, coconut water holds great potential as a feedstock for hydrogen production via water splitting using the photoelectrocatalytic method. Furthermore, its high electrolyte content can enhance the solution's conductivity and act as a natural catalyst during water electrolysis.

Photoelectrocatalytic (PEC) water decomposition from wastewater, a process that uses a photocatalyst-modified electrode, provides a promising method for converting fossil fuels into green hydrogen energy [6]. This method combines electrolysis and photocatalysis to accelerate the separation of water molecules into hydrogen and oxygen [7], [8], [9]. Photocatalyst materials must have high electrical conductivity, good chemical stability, and efficient light-absorbing properties.

Several previous studies indicate that TiO_2, Cu/Ni modified TiO_2, ZnO, and MgO can be used as photocatalysts for hydrogen production via photoelectrocatalytic water splitting [10], [11], [12]. However, these composites are not very practical, as they operate only in the ultraviolet (UV) range, thereby requiring specialized radiation sources. On the other hand, carbon nanomaterial-based photocatalysts can be used as semiconductors, cocatalysts, and support materials [13]. These photocatalysts have a band gap energy in the visible region, around 2.7-2.8 eV, and exhibit high electrical conductivity and good thermal stability [14]. The pure MgO component often exhibits an optical band gap of 3.85-5.0 eV, depending on the preparation method. MgO has good thermal stability and a high adsorption capacity. The combination of carbon and MgO provides unique physical and chemical properties, including good adsorption capacity, making it an ideal candidate for hydrogen production [15]. This composite can enhance electron transfer and light absorption efficiency, as well as accelerate the reaction process on the catalyst surface. Integrating carbon matrices with a MgO photocatalyst significantly narrows the bandgap, reduces electron-hole recombination rates, and expands light absorption into the visible spectrum. Thus, compositing carbon with MgO is expected to yield a photocatalytic composite capable of operating in the visible-light range, with high absorption capacity, high-temperature stability, and high conductivity.

Based on the description above, it can be inferred that the carbon-magnesium oxide (C-MgO) nanocomposites can be used as an electrode modifier composite for hydrogen production from coconut water waste via a photoelectrocatalytic process under visible light irradiation, thereby offering a viable alternative for hydrogen production driven solely by visible light from LED lamps, which are inexpensive and widely available. Therefore, the development of C-MgO nanocomposites is a promising research area in the effort to create an efficient and environmentally friendly green hydrogen production system. To date, no research has investigated C-MgO nanocomposites as electrode modifiers for hydrogen production from coconut water waste via photoelectrocatalysis.

Nanocomposite materials can be synthesized via the hydrothermal method. Hydrothermal carbonization (HTC) represents a promising thermochemical method for converting wet biomass under moderate aqueous conditions into carbon-rich materials [16]. This technique lets scientists control particle size and shape, create very pure, high-quality crystals, and use safe, eco-friendly, water-based solvents without requiring additional high-heat steps. C-MgO nanocomposites can be synthesized using red dragon fruit peel extract via the hydrothermal method [17]. The advantage of this method is that it utilizes high temperature and pressure in water to grow high-purity, well-crystallized nanoparticles with precise control over size, shape, and uniform distribution in a simple, eco-friendly process. This synthesis utilizes the peel's rich content of betacyanins, flavonoids, phenolics, tannins, alkaloids, saponins, and carbohydrates as natural reducing, capping, or stabilizing agents to convert metal ions into stable MgO nanomaterials without hazardous chemicals [17]. Red dragon fruit peel extract, rich in these secondary metabolites, can serve as an eco-friendly reducing agent for the green synthesis of nanomaterials. Therefore, it can be hypothesized that C-MgO

nanocomposites can be synthesized using the same method. This extract, as an agro-industrial waste, contains bioactive compounds that act as proton donors and acceptors and support the principles of green and sustainable technology [18].

Based on the above background, the development of green hydrogen production technology from coconut water via photoelectrocatalysis assisted by C-MgO nanocomposites has great potential for application in Indonesia. Thus, it can be inferred that C-MgO nanocomposites can be synthesized using the hydrothermal method and utilized as electrode-modifying photocatalysts for hydrogen production from coconut water waste via photoelectrocatalysis. The optimal C-MgO composition for hydrogen production via the photoelectrocatalytic splitting of coconut water waste has not yet been reported. Therefore, this research aims to synthesize C-MgO nanocomposites and employ them as electrode-modifying photocatalysts to produce hydrogen from coconut water waste via photoelectrocatalysis. This article reports the results of research on the synthesis of C-MgO nanocomposites through the hydrothermal method for the photoelectrocatalytic production of green hydrogen from coconut water.

2. Research Methodology

2.1. Materials

The materials used are coconut (*Cocos nusifera L.*), red dragon fruit peel (*Hylocereus polyrhizus*), 1.0 M citric acid monohydrate ($C_6H_8O_7.H_2O$) (Emsure Merck 1.00244.1000), 10.0 g urea (CON_2H_4) (Emsure Merck 1.08487.1000), 1.0 M magnesium chloride hexahydrate ($MgCl_2.6H_2O$) (Emsure Merck 1.05833.0250), 1.0 M sodium hydroxide (NaOH) (Emsure Merck 1.06498.1000), distilled water (H_2O), copper film (Cu), 95% ethanol (CH_5OH) (SMART LAB), acetone (C_3H_6O), Whatmann filter paper no.42, mask, and handkerchief. All chemicals are in the pro analysis (PA) category.

2.2. Equipments

The tools used in this study were 50 mL, 100 mL, 250 mL, and 500 mL beakers (Iwaki Pyrex), 10 mL, 50 mL, and 100 mL measuring cups (Iwaki Pyrex), 250 mL and 100 mL measuring flasks (Iwaki Pyrex), microwave ovens (Kirin and Gallenkamp england), dropper pipettes, hot plates, blenders (Mitochiba), 10 mL and 100 mL vials, 100 mL dark bottles, stirring rods, spray bottles, analytical scales (Ohaus Explorer: max 250 g and min 0.001 g), spatulas, funnels, petri dishes (Iwaki Pyrex), sieves (80 and 200 mesh), jars, magnetic stirrers (C-Mag Hs 7), pH meter (WT61), cuvettes, eppendorf tubes, centrifuge (MPW-350), rotary vacuum evaporator, fine cloth, plastic gutter, ruler, 1.5 volt LED lamp, and microwave oven. The instruments used are a UV-Vis Spectrophotometer (Spectroquant Pharo 300 M), Fourier Transform Infrared (FTIR) (Shimadzu), X-Ray Diffraction (XRD) (DW-XRD-2700A), and a hydrogen meter (H2CT-8023).

2.3. Procedures

1) Secondary Metabolite Compounds Extraction

Extraction of organic compounds from red dragon fruit peel is performed by maceration in 96% ethanol at room temperature under light-protected conditions to prevent degradation of active compounds [19]. 1500 grams of red dragon fruit peel simplicia were placed in a 5 L beaker and added to 2500 mL of 96% ethanol. The mixture was macerated for 3 × 24 hours with two stirrings every 24 hours. The mixture was filtered through filter paper to separate the filtrate from the residue. The filtrate was then evaporated using a rotary vacuum evaporator at 40°C for 3 hours to obtain a thick extract.

2) Synthesis of C-MgO Nanocomposites

Synthesis of C-MgO nanocomposites was carried out using a hydrothermal method in three stages. First, synthesis of carbon: 2 g of citric acid monohydrate was mixed with 4 g of urea and 10 mL of red dragon peel extract in 60 mL of distilled water, stirred for 10 minutes, then heated in a microwave oven (500 W, 90 minutes) until carbon powder was formed [20]. Second, synthesis of MgO: 10 mL of red dragon fruit peel extract was put into 60 mL of 0.1 M $MgCl_2$ solution, and 0.5 M NaOH was added drop by drop until the pH reached 12, while stirring at 60°C for 3 hours. The precipitate was then centrifuged and baked in a microwave oven at 60°C for 2 hours, yielding MgO powder. The formation and presence of MgO were confirmed using powder X-ray diffraction (XRD) for the cubic periclase structure and Fourier-transform infrared spectroscopy (FT-IR) for Mg–O stretching vibrations. Next, 1 g of carbon and 1 g of MgO powders were dissolved separately in 50 mL of distilled water while stirring for 30 minutes. Third, for the synthesis of carbon-MgO composites, three 250 mL

beakers were each filled with 80 mL of red dragon fruit peel extract, 50 mL of distilled water, and 10 mL of carbon suspension. Then, 10 mL, 20 mL, and 30 mL of MgO suspension were added to the first, second, and third mixtures, respectively. The mixtures were processed in a hydrothermal reactor at 120°C for 3 hours, then centrifuged and oven-baked for 2 hours, yielding the carbon-MgO nanocomposite [21].

Based on the volume of suspensions, the samples obtained were respectively referred to as 1:1, 1:2, and 1:3 carbon-MgO nanocomposites. Referring to the volume ratio of carbon to MgO, carbon-MgO 2:1 and 3:1 composites were then made. The composition of materials for the synthesis of carbon-MgO mediated by dragon fruit peel extract is presented in Table 1. Based on these data, the carbon concentrations in samples coded 1:1, 1:2, 1:3, 2:1, and 3:1 are 0.11 M, 0.11 M, 0.11 M, 0.22 M, and 0.33 M, respectively. Meanwhile, the MgO concentrations in the same samples are 0.03, 0.06, 0.09, 0.03, and 0.03 M, respectively.

Table 1. Liquid Material Composition for The Synthesis of C-MgO Nanocomposites

Sample Code	C Suspension (mL)	MgO Suspension (mL)	Dragon Peel Extract (mL)	Aquades (mL)
1:1	10	10	80	50
1:2	10	20	80	50
1:3	10	30	80	50
2:1	20	10	80	50
3:1	30	10	80	50

3) Stability and Energy Gap Analysis

Stability analysis of C-MgO composites was performed using a UV-Vis spectrophotometer in the wavelength range of 380–950 nm at time intervals of 0, 10, 20, and 30 minutes to determine the maximum wavelength for each C-MgO composite. The absorbance measurement data across this wavelength range were then tabulated using OriginPro 16 software. The consistency of the wavelength of maximum absorbance across varying measurement times indicates nanoparticle stability.

Next, the energy gap (E_g) was analyzed using a UV-Vis spectrophotometer based on the Diffuse Reflectance UV-Vis (DR UV-Vis) spectrum. The obtained reflectance spectrum was then converted to an equivalent absorption spectrum using the Tauc plot method (Equation 1) [22].

$$(\alpha h\nu)^{1/n} = A(h\nu - E_g) \quad (1)$$

where α is the absorption coefficient, hν is the photon energy, and n defines the transition type. The graph was plotted with $(\alpha h\nu)^{1/n}$ on the y-axis versus $h\nu$ on the x-axis; a tangent line was then extrapolated from the linear region down to the x-axis intercept to determine the E_g value.

4) Chemical Bond Analysis

FTIR characterization aims to identify functional groups or chemical bonds present in the carbon-MgO-red dragon fruit peel extract and in the pure peel extract prepared in powder or film form. The test samples were mixed with KBr powder and pressed into pellets before being analyzed using an FTIR instrument. The absorption spectrum was then measured in the wavenumber range of 4000–450 cm^{-1} with a resolution of 4 cm^{-1} at room temperature.

5) Crystal Structure Analysis

X-ray Diffraction (XRD) analysis was performed to identify the structure and crystallite size of carbon-MgO-red dragon fruit peel extract. Before analysis, the sample surface was coated with amorphous carbon as an in situ matrix or protective layer to prevent MgO grain growth and obtain optimal diffraction results. Next, the sample was inserted into the XRD instrument to scan its diffraction pattern over a scan range (2θ) of 0–100°. The data were then analyzed using Origin Pro 16 software, and the crystal size was calculated using the Debye-Scherrer equation (Equation 2).

$$D = \frac{K\lambda}{\beta \cos \theta} \quad (2)$$

where D is the average crystallite size (nm), K is Scherrer factor (usually 0.9 for spherical particles or the absence of any knowledge of the shape of crystallites), λ is X-ray waavelenght (nm), β is the corrected full width at half maximum (FWHM) or integral breadth (IB) which is in radian, and θ is

the Bragg angle (degree). FWHM or IB is the width of a spectrum curve measured between the background and the peak maximum. The Crystallite size is determined through the following steps: collecting the sample's XRD pattern, identifying angular positions (2θ) and determining θ, measuring the FWHM (β) of prominent diffraction peaks in radians, and applying the Scherrer equation to individual peaks.

6) Preparation of Electrode

A 5x1 cm^2 copper (Cu) film electrode was rubbed with sandpaper to remove impurities and homogenize its surface. The electrode was subsequently coated with C-MgO nanocomposites by immersing a 4 cm section into the material suspension for one hour. The resulting coated electrode was then dried in an oven at 100°C for 20 minutes to ensure the material adhered firmly and evenly. Afterward, the coated electrode was allowed to cool to room temperature. This procedure yielded a nanocomposite-coated Cu film with a dark brown layer approximately 0.5 mm thick, ready for use.

7) Green Hydrogen Production

Green hydrogen production from coconut water was carried out using the photoelectrocatalysis method with the following steps: a carbon-MgO-modified Cu electrode served as the cathode, while a carbon plate served as the anode. Both electrodes were connected to a power supply and immersed in an electrochemical cell containing 500 mL of coconut water. Photoelectrocatalysis was conducted using visible-light radiation from a 1.5-volt LED lamp for 0 to 120 minutes. The ORP value and the concentration (ppm) of generated hydrogen were recorded every 10 minutes, with three repetitions (to determine the average value and its standard deviation), using a hydrogen meter. This duration is sufficient to observe and measure the amount of hydrogen, as well as the trends in ORP values and the concentration of hydrogen produced. The hydrogen meter uses an electrochemical sensor principle with a specialized platinum-based electrode to oxidize dissolved hydrogen molecules (H_2) in water, generating a proportional electrical current that the internal microprocessor converts into a readout of 0-2400 ppb (0-2.4 ppm). The hydrogen meter model CT-8023/H2CT-8023 measures dissolved hydrogen gas (H_2) in an aqueous sample rather than in air. It is primarily used to test hydrogen-rich water generators. In this experiment, hydrogen gas produced by the water-splitting reaction forms at the cathode surface. The same method is used to produce and measure hydrogen from coconut water samples via electrolysis, specifically by splitting water using electrodes without a photocatalytic coating.

The average hydrogen concentration is converted to volume (mL) using the ideal gas equation and then used to determine the green hydrogen production rate via the differential equation (Equation 3).

$$r_{H_2} = \frac{dV}{dt} \tag{3}$$

Where r_{H_2} is the rate of hydrogen production (mL/min). This equation represents the slope of the graph that plots hydrogen gas volume (mL) versus time (minutes).

The portable dissolved hydrogen meter (model **CT-8023/H2CT-8023**) is factory-precalibrated and designed to measure dissolved hydrogen in water (0–2400 ppb). The manufacturer does not outline a routine end-user recalibration process; the unit relies on its fixed sensor electrode, and taking the device apart voids the warranty. If readings become erratic or inaccurate over time, replace the old pen electrode tip rather than attempting a manual calibration.

3. Results and Discussion

3.1. Secondary Metabolite Compounds Extraction

In this study, the maceration method was chosen because it is simple and can maintain the stability of the active compounds. A 96% ethanol solvent is used in the maceration process because it is non-toxic and can dissolve secondary metabolite compounds [23]. Previous research also showed that 96% ethanol has a strong ability to extract anthocyanins, the main pigments in the skin of red dragon fruit [24]. During soaking, the extraction container is covered to protect it from direct light. This process yielded 3000 mL of initial suspension (before evaporation) and 550 mL of final concentrated extract (after evaporation). Based on the volume ratio (v/v) of the extract before and after evaporation, this maceration process yielded a red dragon fruit peel extract suspension of 18.33% (v/v). During

extraction at 40°C, low-boiling-point moisture (water) and residual ethanol are removed by evaporation.

Secondary metabolite compounds act as sensitizers in photocatalytic systems due to their ability to absorb light and transfer energy efficiently. Red dragon fruit peel (*Hylocereus polyrhizus*) extract contains rich secondary metabolites including betalains, flavonoids, phenolics, alkaloids, saponins, and tannins, which deliver powerful antioxidant, antifungal, and anti-inflammatory benefits [25]. In the green synthesis of magnesium oxide nanoparticles using red dragon fruit (*Hylocereus polyrhizus* or *Hylocereus undatus*) peel extract, these compounds act as natural bio-reducing and capping agents. Capping agents help stabilize particles and influence the morphology and size of nanoparticles during the synthesis process [26].

3.2. Hydrothermal Synthesis of Nanocomposites

Hydrothermal treatment is a green chemistry approach because it uses water as a solvent at high temperatures and pressures, making it environmentally friendly and efficient in producing nanoscale materials with good crystallinity. Furthermore, the hydrothermal method allows for control of particle size and morphology [27]. In this study, synthesis of C–MgO nanocomposites was carried out through three main stages, namely carbon, MgO, and C–MgO nanocomposite synthesis, with the addition of red dragon fruit peel extract as a stabilizing agent and sensitizer. A similar concept has been applied in the synthesis of ZnO nanoparticles using red dragon fruit extract [28]. The synthesis mechanism of C-MgO nanocomposites typically involves the thermal decomposition of magnesium precursors ($MgCl_2$) in the presence of a carbon source, leading to nucleation, structural replication, or gas-solid combustion reactions.

The results of this synthesis are shown in Fig. 1, in which the resulting powder is dark gray, indicating the formation of carbon and magnesium oxide phases. Visually, the material samples appear identical. However, optical differences become apparent in the absorbance values of each sample suspension, corresponding to the varying carbon-to-MgO ratios as shown in Fig. 2. The higher the carbon content, the higher its absorbance value. Thus, the sample's dark color is primarily due to the presence of carbon in the composite.

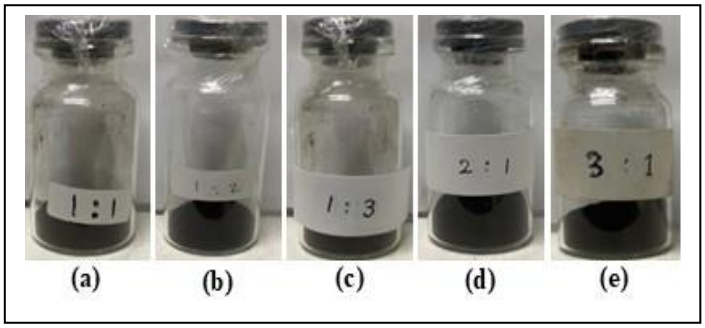

Fig. 1. The synthesis results of C-MgO nanocomposites in the composition of the C-MgO volume ratio: (a) 1:1, (b) 1:2, (c) 1:3, (d) 2:1, and (e) 3:1

3.3. Stability and Energy Gap Analysis

Analysis using a UV-Vis spectrophotometer aims to determine the optical characteristics of carbon-MgO nanocomposite materials, particularly their stability and interaction with light. The purpose of stability determination of the nanocomposite at time intervals of 0, 10, 20, and 30 minutes is to evaluate its colloidal dispersion quality, resistance to aggregation, and temporal degradation over time. The observed phenomenon is related to surface plasmon resonance (SPR), the collective oscillation of electrons on the surface of metal or metal oxide particles when they interact with electromagnetic waves. SPR is an indicator of the formation of nanosized particles because it exhibits a characteristic absorption band at a specific wavelength. Fig. 2 shows the UV-Vis spectrum of C–MgO nanocomposites in the wavelength range of 380–950 nm with the main absorption peak in the 400–500 nm region. Although the maximum wavelengths (λ_{max}) of all nanocomposites appear broad and have significant noise, they are all at consistent wavelengths across all measurement time intervals. No shift in these maximum wavelengths was observed. The consistency of the wavelength, also known as the λ_{SPR}, indicates that particle growth through agglomeration or the formation of a colloidal phase has reached its optimum size. In other words, the absence of a shift in the absorption

peak position at all time intervals indicates that the electronic structure of the material remains stable and that the formed particles do not experience significant changes due to agglomeration or optical degradation during light exposure [29].

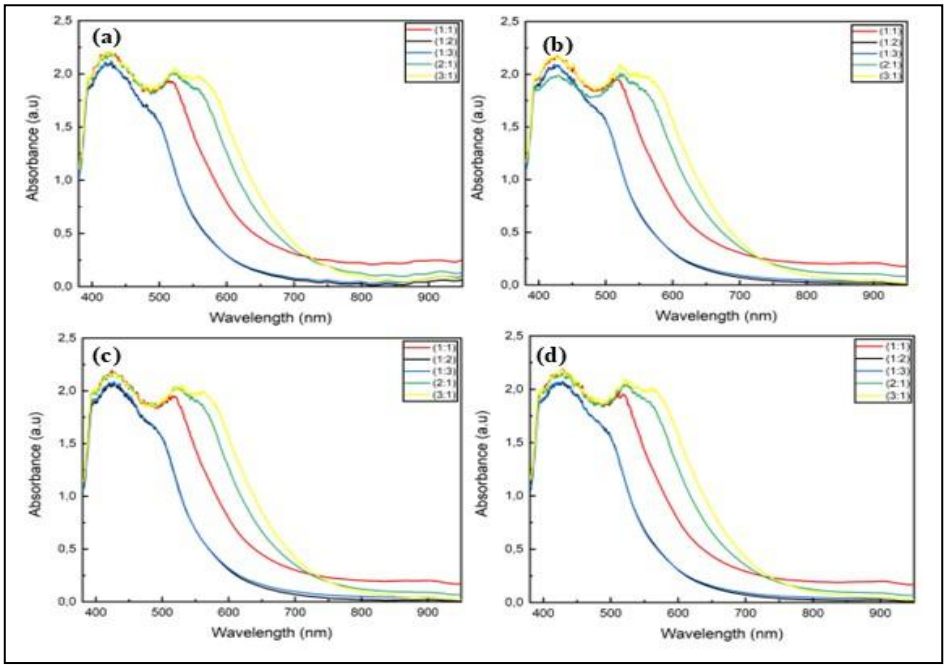

Fig. 2. UV-Vis spectrum of C-MgO material at time intervals of: (a) 0, (b) 10, (c) 20, and (d) 30 minutes

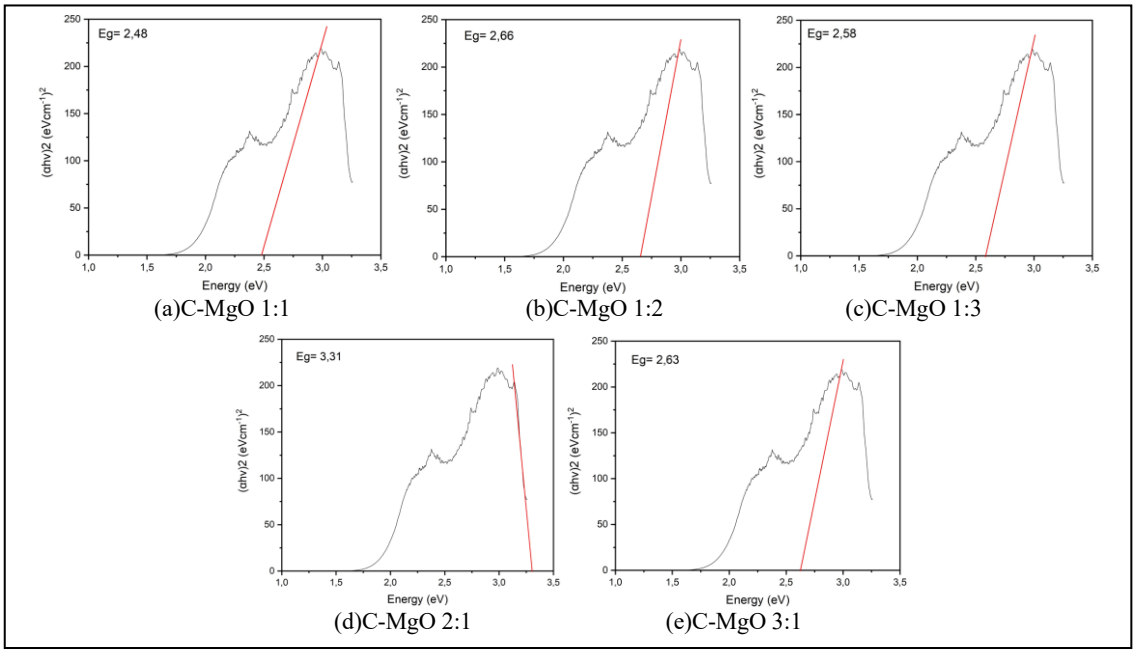

Fig. 3. Band gap energy curves of carbon-MgO

The UV-Vis spectra are also used to determine the band gap energy value of C–MgO materials. The band gap energy is the minimum energy required to excite electrons from the valence band to the conduction band [30]. In this study, the band gap energy was calculated using the indirect transition method ($n = 2$). To calculate the energy gap (Eg) using Equation 1, the absorbance and wavelength data from Fig. 3 were re-tabulated to determine the photon energy ($hv = 1240/\lambda$), with λ in nm, yielding the photon energy in eV. The absorption coefficient (α) was calculated using the equation: $\alpha = 2.303 \times$ absorbance/thickness. Subsequently, a graph was plotted with $(\alpha hv)^{1/n}$ on the y-axis versus hv on the x-axis; a tangent line was then extrapolated from the linear region down to the x-axis intercept to determine E_g. The resulting plot is presented in Fig. 3. The analysis shows that the band gap energies

for the C-MgO samples with ratios of 1:1, 1:2, 1:3, 2:1, and 3:1 are 2.48, 2.66, 2.58, 3.31, and 2.63 eV, respectively. These values indicate that the C-MgO nanocomposite can act as a photocatalyst in the UV and visible regions of the electromagnetic spectrum. The UV-Vis absorption plot used to determine the band gap energy is shown in Fig. 3.

3.4. Chemical Bond Analysis

The FTIR spectrum of the C–MgO nanocomposite shows several distinctive absorption bands (Fig. 4). The broad absorption band at wavenumbers 3427 cm^{-1} indicates the presence of stretching vibrations of the –OH group in phenolic, flavonoid, and anthocyanin compounds in the red dragon fruit peel extract. In carbon-MgO composite materials, the hydroxyl (–OH) stretching absorption band—typically observed around 3443–3485 cm^{-1} in pure MgO or carbon materials—shifts to a lower wavenumber (a red shift). This shift occurs because intermolecular hydrogen bonding and chemical interactions occur between the oxygen/hydroxyl species on the carbon surface and the magnesium or oxide ions in MgO.

The absorption band at a wavenumber of 1622 cm^{-1} is associated with aromatic C=C bonds or conjugated –OH stretching vibrations in the aromatic ring structure of anthocyanin and flavonoid compounds. The presence of this band indicates that some organic compounds in the extract interact with the surface of the MgO material [31]. In C-MgO composite materials, the infrared absorption band for the skeletal C=C stretching vibration typically appears around 1580 – 1620 cm^{-1} (inherited from the graphitic or aromatic carbon network). Compared to pure carbon materials, this C=C band exhibits a minor shift (often a slight upward or downward displacement of 5–20 cm^{-1} or broadening), driven by interfacial electron transfer and weak electrostatic or coordination interactions with the MgO surface. In contrast, pure MgO itself lacks organic C=C bonds and only shows distinct metal-oxygen (Mg-O) stretching below 700 cm^{-1}.

In addition, the absorption band at wavenumber 1421–1425 cm^{-1} indicates the presence of stretching vibrations of the C–O group or carbonate ion (CO_3^{2-}). This group can form during the oxidation of certain organic compounds during thermal synthesis, producing carbonate byproducts. This C–O group contributes to increased surface stability and bond strength between the carbon phase and MgO. The presence of the MgO component in the nanocomposite is evident from the strong absorption band associated with the stretching vibration of the Mg–O bond at wavenumbers 520–559 cm^{-1}. Thus, the FTIR analysis proves that the C–MgO nanocomposite successfully forms a strong chemical bond between the two components.

In C–MgO composite materials, the characteristic Mg–O stretching absorption band generally exhibits a lack of drastic or significant shift in its peak position compared to pure MgO (which typically appears around 410-540 cm^{-1}, depending on particle size and morphology). Instead, the interaction with the carbon matrix primarily causes peak broadening, attenuation, or minor variations rather than a major shift in wavenumber. FTIR spectra of C-MgO 1:1; 1:2; 1:3; 2:1; and 3:1 nanocomposites are shown in Fig. 4, while FTIR peak assignments for the C-MgO samples, pure MgO, and pure C are summarized in Table 2.

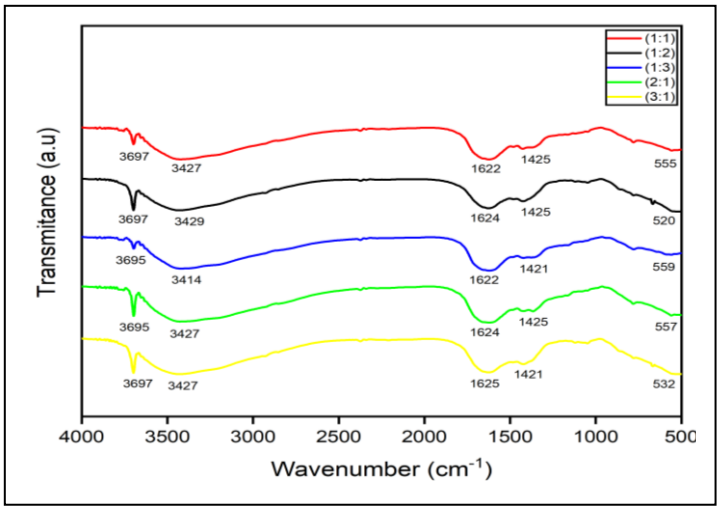

Fig. 4. FTIR spectrum of C-MgO nanocomposites

Table 2. FTIR Peak Assignments for the C-MgO samples, Pure MgO, and Pure C

Band attributed (cm^{-1})				Phenomenon	Description
C-MgO Composite		*Pure MgO*	*Pure C*		
3427	3448 [32]	3443–3485	3420–3436	O–H stretch (hydroxyl)	Phenolic, flavonoid, and anthocyanin O–H stretching vibrations
1622	1637 [33]	-	1600– 1623	C=C stretch	Aromatic ring vibrations
1421–1425	1399 [34]	-	1000–1200	C–O stretch	Carboxylic functional group
520–559	617, 534 [35]	410–540	-	Mg–O stretch	Presence of MgO particles

3.5. Crystal Structure and Size Analysis

XRD Analysis was carried out to identify the crystal structure, determine the crystallite size, and assess the degree of crystallinity and the phases formed in the carbon–MgO–red dragon fruit peel extract. The XRD diffraction pattern of the carbon–MgO material is shown in Fig. 5. The sharp diffraction peaks detected at peak positions (2θ) of 18.5°, 31.8°, 38.0°, and 45.5° are attributed to the (111), (200), (220), (311), and (222) planes of cubic MgO, respectively. The XRD spectrum shows a shift in the MgO 2θ peak position between this study's results and the reference data (Fig. 5). The shift in the 2θ-peak positions of an MgO XRD spectrum from its standard positions is mainly caused by lattice strain (from stress or defects), compositional changes (from solid solution/doping), instrumental errors (like sample displacement), or temperature changes (thermal expansion). Crystal planes resemble the crystal phase of JCPDS Card No. 97–7746. A sharp and intense peak is observed in the XRD spectrum around (200), which proves the high crystallinity of MgONPs [36]. Spectral peaks at the other 2 positions with relatively high intensities likely originate from particles not identified in this study. In addition, a weak peak at 2θ = 26.2° also appears, indicating the presence of a graphitic carbon phase, which most likely originates from organic compounds in the red dragon fruit peel extract that undergo carbonization. The absence of a shift in the position of the main MgO peak after the addition of the extract indicates that the carbon does not replace Mg or O atoms in the MgO crystal lattice, but only coats the particle surface as an amorphous layer.

Adding carbon to a C-MgO composite typically does not disrupt the fundamental cubic crystal structure of the periclase (MgO) phase. Still, it influences crystallite size growth, peak broadening, and overall matrix dispersion. The results of crystallite size analysis using the Debye–Scherrer equation showed a decrease in crystallite size from 17.93 nm (MgO-Extract) to 17.41 nm (C-MgO-Extract). This indicates that the addition of carbon can inhibit the growth of MgO crystals and produce smaller, nanosized crystallites because carbon atoms are smaller than magnesium atoms. This growth-inhibitory effect is also caused by secondary metabolites such as anthocyanins, flavonoids, and phenolics, which act as capping agents. These compounds can attach to the particle surface and form a protective layer that prevents particle aggregation, thereby controlling crystal growth and maintaining particle size on a nanometer scale. XRD spectrum of the C-MgO nanostructure is shown in Fig. 5. At the same time, the calculated crystallite size data of MgO and C-MgO 1:3 composites, based on the 4 curves with the highest intensity, are presented in Table 3.

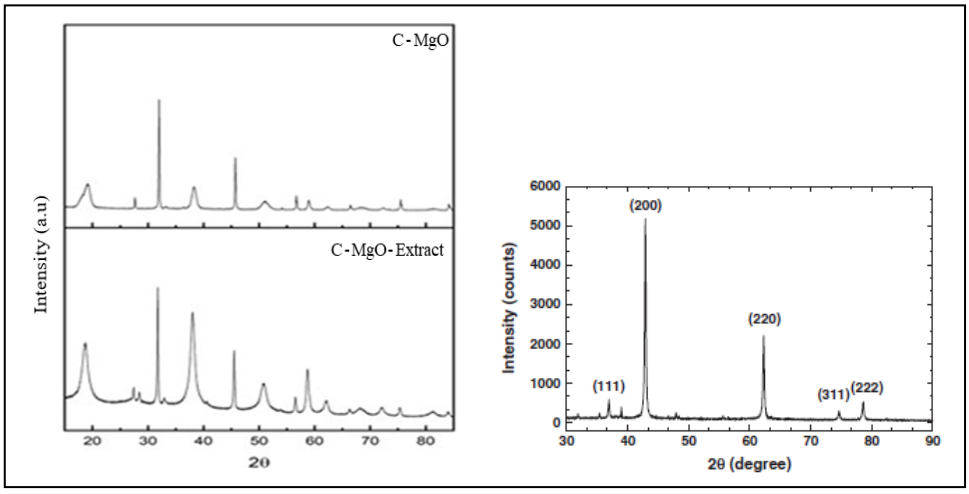

Fig. 5. XRD spectrum of (a) MgO and carbon-MgO nanostructures observed and (b) MgO presented in reference [37].

Table 3. Crystallite Size of MgO and C-MgO 1:3 Composites

Peak Position (2θ) (Radians)	(hkl)	FWHM (Radians)	X-Ray Wavelength (nm)	Crystallite Size (nm)	Crystallite Size Average (nm)
			C-MgO 1:3		
18.5	(111)	0.5	0.15418	16.83	17.41 ± 0.429
31.8	(200)	0.5	0.15418	17.27	
38.0	(220)	0.5	0.15418	17.56	
45.5	(311)	0.5	0.15418	18.01	
			MgO		
19.0	(111)	0.5	0.15418	16.84	17.93 ± 1.046
32.0	(200)	0.5	0.15418	17.28	
38.5	(220)	0.5	0.15418	19.59	
45.6	(311)	0.5	0.15418	18.02	

3.6. Green Hydrogen Production

In this study, hydrogen production was achieved via photoelectrocatalysis of coconut water, with a carbon plate as the anode and a C-MgO nanocomposite-modified electrode as the cathode. During the process, the electrochemical cell was illuminated with a 1.5-volt LED lamp. The electrolysis was run at 12 V for 120 minutes. In the photoelectrocatalysis system, a power supply provides the potential difference required to decompose water molecules into H_2 and O_2 gases. An LED lamp provides visible light to activate the catalyst during electrophotocatalysis.

The use of the C–MgO catalyst aims to accelerate the water-splitting reaction. This catalyst has two main components that work synergistically: carbon acts as an electrical conductor, facilitating electron transfer, while MgO serves as a catalytic active site, facilitating redox reactions during photoelectrocatalysis. Furthermore, active compounds act as photosensitizers, increasing light absorption and facilitating electron excitation on the catalyst surface. Based on the C-MgO band gap energy obtained in this study (Table 1), the photoelectrocatalysis process can be carried out across the UV-visible region. Reaction process occurs in three steps: first, when semiconductor exposed to light, electrons (e^-) are excited from valence band (VB) to conduction band (CB), leaving holes (h^+) in the VB; second, e^- and h^+ migrate to the photocatalyst surface; and finally, e^- and h^+ simultaneously participate in the reduction of H^+ to produce H_2 and the oxidation of H_2O to produce O_2 [38]. The electrochemical reactions in the photoelectrocatalysis process are shown in Equations 4-7 [39].

The catalyst absorbs light:

$$\text{C-MgO} + h\nu \rightarrow e^- + h^+ \quad (4)$$

½-reaction of oxidation:

$$2H_2O(aq) + 4h^+ \rightarrow O_2(g) + 4H^+(aq) \quad (5)$$

½-reaction of reduction:

$$4H^+(aq) + 4e^- \rightarrow 2H_2(g) \quad (6)$$

Overall reaction:

$$2H_2O(aq) \rightarrow 2H_2(g) + O_2(g) \quad E^o = 1{,}23 \text{ eV}; \Delta G^0 = 237{,}2 \text{ kJ mol}^{-1} \text{ [40]} \quad (7)$$

One of the photocatalytic mechanisms of water during the photoelectrocatalysis of coconut water is shown in Fig. 6 [39]. Based on this study, the C-MgO photocatalyst has a band gap energy of 2.48–2.63 eV. Because C-MgO has a band gap energy greater than 1.23 eV, this composite can catalyze hydrogen production during the photoelectrocatalysis of coconut water samples [39].

Oxidation-Reduction Potential (ORP) and hydrogen production are directly linked: producing molecular hydrogen (H_2) injects electrons into a solution, creating a strong reducing environment that shifts the ORP value from positive to negative. Lower or more negative ORP values generally indicate a higher concentration of free hydrogen, though ORP measures overall electron activity rather than exact hydrogen concentration. In this study, the negative ORP values observed during hydrogen

production, both without and with C-MgO-modified electrodes, indicate that hydrogen production from the electrolysis and photoelectrocatalysis of coconut water is not spontaneous (Table 2).

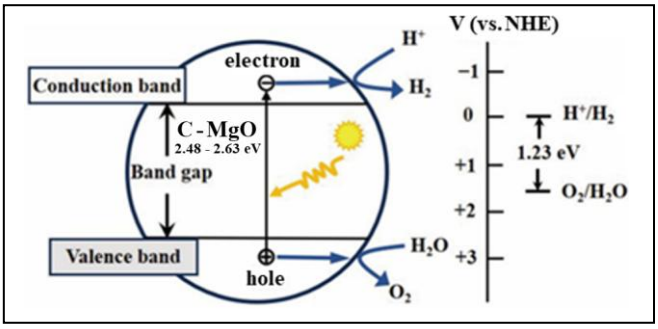

Fig. 6. Band gap energy diagram of the C-MgO photocatalyst for hydrogen evolution from water splitting via photoelectrocatalysis

The ORP value with unmodified electrodes (electrolysis) is much more negative than that with C-MgO-modified electrodes (photoelectrocatalysis), indicating that hydrogen production via electrolysis requires much more energy than via photoelectrocatalysis. According to previous research, an ORP value of around –150 mV to –300 mV is sufficient to support efficient hydrogen production [41]. Therefore, the ORP value in this study indicates that the carbon–MgO photocatalyst is suitable for photoelectrocatalytic hydrogen production. In addition, the longer the electrochemical process, the greater the volume (*V*) of hydrogen gas produced, as the reaction proceeds in one direction without inhibition by reaction products (Table 4).

Table 4. Oxidation-Reduction Potential (mV) and Volume (mL) of Hydrogen Production

Time (min)	Without C-MgO		C-MgO 1:1		C-MgO 1:2		C-MgO 1:3		C-MgO 2:1		C-MgO 3:1	
	ORP	***V***	***ORP***	***V***	***ORP***	***V***	***ORP***	***V***	***ORP***	***V***	***ORP***	***V***
0	0	0	0	0	0	0	0	0	0	0	0	0
20	-687	0.44	-155	1.64	-225	2.16	-241	1.68	-277	2.55	-361	1.48
40	-720	0.67	-212	2.57	-336	3.19	-328	8.14	-350	3.16	-381	2.30
60	-794	0.82	-313	3.79	-395	4.23	-469	10.28	-496	4.01	-414	2.65
80	-861	1.09	-470	4.55	-542	5.09	-495	12.4	-568	4.26	-422	3.18
100	-901	1.78	-554	6.11	-704	6.32	-632	16.23	-598	4.95	-516	3.32
120	-912	2.36	-639	7.03	-963	8.25	-680	18.27	-630	5.64	-629	5.32

In this study, the volume of hydrogen gas produced over 0-120 minutes was used to calculate the hydrogen production rate (Equation 3) by determining the slope of the curve representing the change in hydrogen volume over the given time interval during the water-splitting reaction. The actual volume of hydrogen produced during the electrolysis and photoelectrocatalysis processes is presented in Table 3. The highest volume of hydrogen (8.25 mL) was produced by photoelectrocatalysis using a C-MgO 1:2 composite over 120 minutes. The hydrogen production rate curve is shown in Fig. 7. Based on the slope of the curve, the hydrogen gas production rate from the electrolysis process (water splitting using an uncoated nanomaterial electrode) is only 0.3636 mL/min. Hydrogen production via the photoelectrocatalytic process occurs at a higher rate than the electrolytic process, with rates ranging from 1.1432 mL/min to 3.1498 mL/min (for varying MgO amounts) and from 0.7329 mL/min to 1.1432 mL/min (for varying carbon amounts). The effect of increasing the amount of MgO on the photoelectrocatalytic hydrogen production rate is greater than that of increasing the amount of carbon in the composite. Increasing the MgO and carbon content in the nanocomposites can increase the hydrogen production rate to 3.1489 mL/minute (766.03%) (Fig. 7.a). Specifically, the mechanism of hydrogen production via photoelectrocatalytic water splitting is outlined in Equations 4–7 and Fig. 6. Exposure to visible light from an LED lamp excites electrons from the valence band (VB) to the conduction band (CB) at the surface of the C-MgO nanocomposites. The migrating electron$^-$ leaves an electron vacancy, or hole (h+), in the VB. Once charge separation is maintained, the light-generated electron travels to the catalyst surface, thereby accelerating the water-splitting reaction into hydrogen at the cathode and oxygen at the anode.

In C-MgO composites, interfacial chemical bonds (such as Mg-O-C) and oxygen-containing functional groups (like -COOH and -OH) dramatically improve photoelectrocatalytic (PEC) water splitting by accelerating charge separation, lowering overpotentials, and enhancing active site availability [42], [43]. Surface polar groups (-OH, C=O, -COOH) enhance wettability, concentrating water molecules (H_2O) directly onto active catalytic sites. Functionalization and intrinsic carbon defects act as trapping centers that favorably adjust the hydrogen adsorption free energy (ΔG_H), boosting overall reaction kinetics. This study shows that C-MgO composites, with a band gap energy of 2.48-2.63 eV, can be used as electrode modifiers to accelerate the green hydrogen production process via photoelectrocatalysis.

As with other photocatalytic materials, photocatalytic performance is influenced by crystallite size [44]. In carbon-supported MgO composite systems, smaller crystallite sizes (typically 5–20 nm) significantly shorten bulk charge-carrier diffusion lengths, increase the active electrochemical surface area, and optimize heterojunction interfaces, thereby enhancing water-splitting reactions. Smaller crystallites expand the specific surface area, exposing more active edge and corner sites for the oxygen/hydrogen evolution reactions (OER/HER). Reduced crystallite dimensions minimize the distance photogenerated electrons and holes must travel to reach the surface, suppressing bulk recombination. When MgO domains are uniformly dispersed on carbon networks, small crystallites ensure seamless interfacial contact, promoting local electric fields and rapid electron transfer. A comparison of the hydrogen gas volumes produced via electrolysis and photoelectrocatalysis is presented in Table 5.

Table 5. The Volume of Hydrogen Produced During Electrolysis and Photoelectrocatalysis

Time (minutes)	Volume of Hydrogen (mL)					
	Electrolysis	*Photoelectrocatalysis*				
		C-MgO 1:1	*C-MgO 1:2*	*C-MgO 1:3*	*C-MgO 2:1*	*C-MgO 3:1*
0	0.00	0.00	0.00	0.00	0.00	0.00
20	0.44	1.64	2.16	1.68	2.55	1.48
40	0.67	2.57	3.19	8.14	3.16	2.30
60	0.82	3.79	4.23	10.28	4.01	2.65
80	1.09	4.55	5.09	12.40	4.26	3.18
100	1.78	6.11	6.32	16.23	4.95	3.32
120	2.36	7.03	8.25	18.27	5.64	5.32

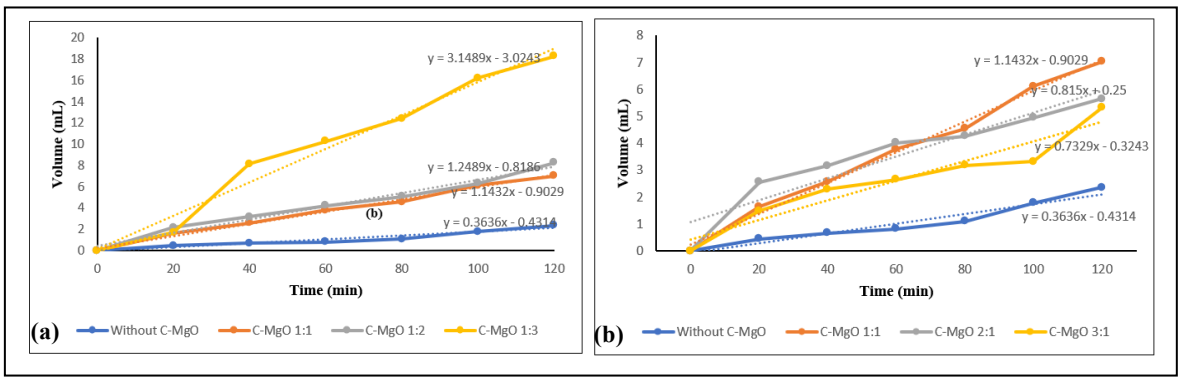

Fig. 7. Rate of hydrogen formation (indicated by the slope value of each curve) through the photoelectrocatalysis method based on: (a) MgO and (b) carbon variations

4. Conclusion

The carbon-magnesium oxide composite was successfully synthesized through the hydrothermal method and demonstrated good stability. The UV-Vis spectrophotometric results showed that C–MgO absorbed visible light, with a band gap energy of 2.48-2.66 eV. This energy is sufficient to drive the photoelectrocatalytic splitting of water into hydrogen and oxygen under visible radiation. FTIR analysis indicated the absorption bands of –OH, aromatic C=C, carboxylic C–O, and Mg–O at wavenumbers of 3427, 1622, 1421–1425, and 520–559 cm^{-1}, respectively. These interfacial chemical bonds and oxygen-containing functional groups improve photoelectrocatalytic water splitting. The

XRD pattern showed that C-MgO has a cubic crystal structure with an average crystallite size of 17.41 nm. A C-MgO composite with such a crystal size can enhance the water-splitting reaction via a photoelectrocatalytic process under visible-light irradiation. The electrolysis process (without a C-MgO catalyst) produces hydrogen from a coconut water sample at a rate of 0.3636 mL/min. Compared with the production rate via electrolysis, the hydrogen production rate for the same sample via photoelectrocatalysis using the C-MgO photocatalyst is significantly higher, reaching up to 3.1489 mL/min (766.03%). It can be concluded that C-MgO composites can be used to enhance the hydrogen production rate via photoelectrocatalysis under visible light irradiation.

Notation

$F(R_\infty)$ = Kubelka–Munk function
R_∞ = reflectance value
α = molar absorption coefficient
S = scattering coefficient
h = Planck's constant
= 6.62607015×10^{-34} m^2 kg/s
v = frequency (Hz)
D = average crystallite size (nm)
λ = X-ray wavelength = 1.5406 Å
β = FWHM or IB value of the dominant diffraction peak, corrected in radians
θ = Bragg angle (degrees)
K = Scherrer constant = 0.94
r_{H_2} = rate of hydrogen production (mL/min)
V = volume (mL)
t = time (minutes

Acknowledgment

Special thanks to the Directorate General of Higher Education, Ministry of Higher Education, Science and Technology, for the research funding grant under the Research Program Implementation, decision no. 995/B2/DT.01.00/2025.

References

[1] M. H. Cavalcanti, J. R. Pappalardo, L. T. Barbosa, P. P. F. Brasileiro, B. A. C. Roque, N. M. P. da R. Silva, M. F. da Silva, A. Converti, C. M. B. de M. Barbosa, and L. A. Sarubbo, "Hydrogen in Burners: Economic and Environmental Implications," *Multidisciplinary Digital Publishing Institute (MDPI)*, vol.12, no. 2434, pp. 1-46, Nov. 01, 2024, doi: 10.3390/pr12112434.

[2] V. K. Mittal and N. Singh, "Comparative Study and Data Analysis of Combustive Properties of Hydrogen Fuel and Other Conventional Fuels," *International Journal of Engineering Research & Technology (IJERT),* vol. 5, issue 05, pp. 1-4, 2917, www.ijert.org.

[3] N. H. Merabet, K. Kerboua, and J. Hoinkis, "Hydrogen Production from Wastewater: A Comprehensive Review of Conventional and Solar Powered Technologies," *Renewable Energy,* Elsevier Ltd., vol. -, no. -, pp. 1-16, May 01, 2024, doi: 10.1016/j.renene.2024.120412.

[4] K. K. Tin, W. Taweepreda, and A. Kumar, "Current Trends and Future Prospects of Hydrogen Production from Coconut Waste," *Int. J. Hydrogen Energy*, vol. 164, no. -, pp. 1–17, Sep. 2025, doi: 10.1016/j.ijhydene.2025.150782.

[5] S. Shi, W. Wang, F. P. Wang, H. Yang, X. He, and X. Liao, "Research Progress in Coconut Water: A Review of Nutritional Composition, Biological Activities, and Novel Processing Technologies," *Multidisciplinary Digital Publishing Institute (MDPI),* Basel, Switzerland, vol. 14, no. -, pp. 1-30, April 25, 2025, doi: 10.3390/foods14091503.

[6] A. Rioja-Cabanillas, D. Valdesueiro, P. Fernández-Ibáñez, and J. A. Byrne, "Hydrogen from Wastewater by Photocatalytic and Photoelectrochemical treatment," *J. Phys. Energy*, IOP Publishing Ltd., vol. 3, no. -, pp. 1-21, Jan. 01, 2021, doi: 10.1088/2515-7655/abceab.

[7] M. Santoso and N. Hamidi, "Pengaruh Cahaya Merah Terhadap Produksi Hidrogen Pada Proses Elektrolisis," *Prosiding KONSTELASI,* vol. 2 no.1, Juni 2025

[8] F. Qiao, "Photoelectrocatalytic Hydrogen Production: Hydrogen Production Principle, Performance Optimization Strategy, Application and Prospect," *Nano Research Energy, Tsinghua University Press*., vol. 4, no. -, pp. 1-25, Mar. 01, 2025, doi: 10.26599/NRE.2024.9120132.

[9] L. Clarizia, M. N. Nadagouda, and D. D. Dionysiou, "Recent Advances and Challenges of Photoelectrochemical Cells for Hydrogen Production," *Elsevier B.V.*, vol. 41, no. -, pp. 1-12, Jun. 01, 2023, doi: 10.1016/j.cogsc.2023.100825.

[10] M. Bouchabou, J. M. Rives López, M. del C. Román Martínez, and M. A. Lillo-Rodenas, "Evaluating H2 Production by Ultraviolet-Induced Water Splitting over (Cu or Ni)-TiO2 Nanoparticle Photocatalysts," *ACS Appl. Nano Mater.*, vol. 8, no. 17, pp. 8646–8662, May 2025, doi: 10.1021/acsanm.5c00100.

[11] S. I. Al-Saeedi, "Photoelectrochemical Green Hydrogen Production Utilizing ZnO Nanostructured Photoelectrodes," *Micromachines (Basel).*, vol. 14, no. 5, pp. 1–18, May 2023, doi: 10.3390/mi14051047.

[12] S. Shanmugaratnam, D. Velauthapillai, P. Ravirajan, A. A. Christy, and Y. Shivatharsiny, "CoS2/TiO2 Nanocomposites for Hydrogen Production under UV Irradiation," *Materials*, vol. 12, no. 23, pp. 1–9, Dec. 2019, doi: 10.3390/MA12233882.

[13] M. A. Rasool, R. Sattar, A. Anum, S A. Al-Hussain, S. Ahmad, A. Irfan, and M. E. A. Zaki, "An Insight into Carbon Nanomaterial-Based Photocatalytic Water Splitting for Green Hydrogen Production," *Catalysts*, *MDPI*., vol. 13, no. -, pp. 1-31, Jan. 01, 2023, doi: 10.3390/catal13010066.

[14] S. H. Mahmoud and A. M. M. El-Tanahy, "Effect of Carbon Nanoparticles in Biochar and Sulphur as a Foliar Spray on Onion Plants: A New Orientation," *Gesunde Pflanzen*, vol. 75, no. 4, pp. 1361–1368, Aug. 2023, doi: 10.1007/s10343-022-00768-2.

[15] S. Yan, L. Wei, Y. Gong, and K. Yang, "Enhanced Hydrogen Storage Properties of Magnesium Hydride by Multifunctional Carbon-based Materials: A review," *International Journal of Hydrogen Energy*, Elsevier Ltd., vol. 55, no. -, pp. 521-541, Feb. 15, 2024, doi: 10.1016/j.ijhydene.2023.11.219.

[16] H. Durak, R. Z. Yarbay, and B. Atilgan Türkmen, "Hydrothermal Carbonization of Biomass for Hydrochar Production: Mechanisms, Process Parameters, and Sustainable Valorization," *Processes*, *Multidisciplinary Digital Publishing Institute (MDPI)*, vol. 14, no. 339, pp. 1-63, Jan. 01, 2026, doi: 10.3390/pr14020339.

[17] Z. F. Mahdi, H. J. M. Altameme, and N. K. Radi, "Renewable Dragon Fruit Peel Extract-Based Magnesium Oxide Nanoparticle Synthesis and Burn-Related Pseudomonas Aeruginosa Antibacterial and Antioxidant Features," *Journal of Nanostructures*, vol. 16, no. 3, pp. 3323–3336, Jul. 2026, doi: 10.22052/JNS.2026.03.026.

[18] Z. Chen, B. Zhong, C. J. Barrow, F. R. Dunshea, and H. A. R. Suleria, "Identification of phenolic compounds in Australian grown dragon fruits by LC-ESI-QTOF-MS/MS and determination of their antioxidant potential," *Arabian Journal of Chemistry*, vol. 14, no. 6, Jun. 2021, doi: 10.1016/j.arabjc.2021.103151.

[19] R. G. P. Panjaitan and Novitasari, "Anti-diabetic activity of the Red Dragon Fruit Peel (Hylocereus polyrhizus) in ethanol extract against diabetic rats," *Pharmacognosy Journal*, vol. 13, no. 5, pp. 1079–1085, Sep. 2021, doi: 10.5530/pj.2021.13.140.

[20] A. B. Aritonang, A. Sapar, H. P. Sari, P. Ardiningsih, and A. Adhitiyawarman, "Synthesis and Characterization of SCDs/TiO2 Composite," *CHEESA: Chemical Engineering Research Articles*, vol. 5, no. 2, p. 92, Dec. 2022, doi: 10.25273/cheesa.v5i2.13915.92-100.

[21] M. Kumar, N. Kumar Singh, R. Sharath Kumar, and R. Singh, "Production of Green Hydrogen through Photocatalysis," 2024. [Online]. Available: https://pubs.acs.org/sharingguidelines

[22] P. Makuła, M. Pacia, and W. Macyk, "How To Correctly Determine the Band Gap Energy of Modified Semiconductor Photocatalysts Based on UV-Vis Spectra," *J. Phys. Chem. Lett*., *American Chemical Society*, vol. 9, no. -, pp, 6814−6817, Dec. 06, 2018, doi: 10.1021/acs.jpclett.8b02892.

[23] Y. D. Muksin, Mahrus, and S. Bahri, "Exploring The Phytochemical and Antioxidant Potential of Hylocereuspolyrhizus Peel Extract Using Biochemical Approach," *IOP Conf. Series: Earth and Environmental Science,* IOP Publishing Ltd., vol. -, no. -, pp. 1-6, Dec. 02, 2021, doi: 10.1088/1755-1315/913/1/012076.

[24] R. S. Salsabila, T. Pambudi, M. S. Perdani, and F. Yuliasari, "KARAKTERISTIK PIGMEN ANTOSIANIN DARI EKSTRAK KOL UNGU (BRASSICA OLERACEA) DAN UBI JALAR UNGU (IPOMEA BATATAS L.POIR) SEBAGAI ZAT WARNA PENYERAP CAHAYA UNTUK SEL

SURYA JENIS DYE-SENSITIZED SOLAR CELL (DSSC) ABSTRACT," *JoP*, vol. 10, no. 3, pp. 60–66, 2025.

[25] R. Hendra, L. Masdeatresa, M. Almurdani, R. Abdulah, and Y. Haryani, "Antifungal Activity of Red Dragon Peel (Hylocereus polyrhizus)," in *IOP Conference Series: Materials Science and Engineering*, Institute of Physics Publishing, Jun. 2020, pp. 1–4. doi: 10.1088/1757-899X/833/1/012014.

[26] Z. Villagrán, L. M. Anaya-Esparza, C. A. Velázquez-Carriles, J. . Silva-Jara, J. M. Ruvalcaba-Gómez, E. F. Aurora-Vigo, E. Rodríguez-Lafitte, N. Rodríguez-Barajas, I. Balderas-León, and F. Martínez-Esquivias, "Plant-Based Extracts as Reducing, Capping, and Stabilizing Agents for the Green Synthesis of Inorganic Nanoparticles," *Resources*, *Multidisciplinary Digital Publishing Institute (MDPI)*, vol. 13, no. 70, pp. 1-24, Jun. 01, 2024, doi: 10.3390/resources13060070.

[27] Y. X. Gan, A. H. Jayatissa, Z. Yu, X. Chen, and M. Li, "Hydrothermal Synthesis of Nanomaterials," *Journal of Nanomaterials*, Hindawi, vol. -, no. -, pp. 1-3, 2020.

[28] N. Sakulpeeb, W. Koetniyom, S. Chutipaijit, S. Rahong, N. Kayunkid, A. Rangkasikorn, S. Wirunchit, and J. Nukaew, "Influence of Dragon Fruit Peels on the Synthesis of Antibacterial Nano Zinc Oxide (Nano-ZnO) via Green Synthesis Method," *Curr. Appl. Sci. Technol.*, vol. 26, no. 4, e0263969, pp. 1-10, Oct. 2025, doi: 10.55003/cast.2025.263969.

[29] L. Haiden, M. Feuchter, A. J. Brunner, M. Barbezat, A. Pansare, B. Ravindran, V. Terziyska, and G. Pinter, "Shining a Light on Carbon-Reinforced Polymers: Mg/MgO and TiO_2 Nanomodifications for Enhanced Optical Performance," *Journal of Composites Science*, vol. 9, no. 4, pp. 1-19, Apr. 2025, doi: 10.3390/jcs9040187

[30] D. Rahmayanti, P. Manurung, and R. Marjunus, "Perbandingan Aktifitas Fotokatalis Nanotitania Tanpa Dan Dengan Penambahan Etanolamina Di Bawah Sinar Matahari," 2023.

[31] Z. Ding and A. Selloni, "Hydration structure of flat and stepped MgO surfaces," *Journal of Chemical Physics*, vol. 154, no. 11, Mar. 2021, doi: 10.1063/5.0044700.

[32] R. B. Rotti *et al.*, "Green Synthesis of MgO Nanoparticles and Its Antibacterial Properties," *Front. Chem.*, vol. 11, pp. 1–13, 2023, doi: 10.3389/fchem.2023.1143614.

[33] C. Valencia, C. H. Valencia, F. Zuluaga, M. E. Valencia, J. H. Mina, and C. D. Grande-Tovar, "Synthesis and application of scaffolds of chitosan-graphene oxide by the freeze-drying method for tissue regeneration," *Molecules*, vol. 23, no. 261, pp. 1-16, Oct. 2018, doi: 10.3390/molecules23102651.

[34] S. Rao, J. Upadhyay, K. Polychronopoulou, R. Umer, and R. Das, "Reduced Graphene Oxide: Effect of Reduction on Electrical Conductivity," *Journal of Composites Science*, vol. 2, no. 2, pp. 1–12, Jun. 2018, doi: 10.3390/jcs2020025.

[35] S. Sagadevan *et al.*, "Effect of Synthesis Temperature on the Morphologies, Optical and Electrical Properties of MgO Nanostructures," *J. Nanosci. Nanotechnol.*, vol. 20, no. 4, pp. 2488–2494, Sep. 2019, doi: 10.1166/jnn.2020.17185.

[36] A. Muhaymin, H. E. A. Mohamed, K. Hkiri, A. Safdar, S. Azizi, and M. Maaza, "Green synthesis of magnesium oxide nanoparticles using Hyphaene thebaica extract and their photocatalytic activities," *Sci. Rep.*, vol. 14, no. 1, pp. -, Dec. 2024, doi: 10.1038/s41598-024-71149-0.

[37] T. Somanathan, V. M. Krishna, V. Saravanan, R. Kumar, and R. Kumar, "MgO Nanoparticles for Effective Uptake and Release of Doxorubicin Drug: PH Sensitive Controlled Drug Release," *J. Nanosci. Nanotechnol.*, vol. 16, no. 9, pp. 9421–9431, Sep. 2016, doi: 10.1166/jnn.2016.12164.

[38] X. Li, C. Zhang, J. Geng, S. Zong, and P. Wang, "Photo(electro)catalytic Water Splitting for Hydrogen Production: Mechanism, Design, Optimization, and Economy," *Molecules, Multidisciplinary Digital Publishing Institute (MDPI)*, vol. 30, no. 630, pp. 1-47, Feb. 01, 2025, doi: 10.3390/molecules30030630.

[39] Z. Wang, T. Hisatomi, R. Li, K. Sayama, G. Liu, K. Domen, C. Li, and L. Wang, "Efficiency Accreditation and Testing Protocols for Particulate Photocatalysts toward Solar Fuel Production," *Joule*, Cell Press. Vol. 5, no. -, pp. 344-359, Feb. 17, 2021, doi: 10.1016/j.joule.2021.01.001.

[40] S. Ha, D. Oh, D. Choi, K. Veeramani, S. Surendran, D. J. Moon, G. H. Jeong, J. Kim, X. Lu, H. Choi, G. Kwon, Y. Yun, and U. Sim, "Carbon-based Catalysts for Photoelectrochemical Water Splitting:

Advancing Carbon–neutral Hydrogen Production," *Carbon Neutrality, Springer*, vol. 4, no. 38, pp. 1-19, Dec. 01, 2025, doi: 10.1007/s43979-025-00150-x.

[41] E. Reszke, G. Binkiewicz, and G. Schroeder, "Process Technology for Production of Hydrogen-Rich Water and Water Characterizing by Highly Negative Oxidation Reduction Potential," *Asian Journal of Applied Chemistry Research*, vol. 12, no.1, pp. 41–55, Oct. 2022, doi: 10.9734/ajacr/2022/v12i1214.

[42] X. Su, N. Cao, J. Feng, W. Li, X. Ding, Z. Li, M. Gao, L. Hu, H. Zhang, Y. Ren, T. Wei, "The Enhanced Photocatalytic Performance of The Amorphous Carbon/MgO Nanofibers: Insight Into The Role of The Oxygen Vacancies and 1D Morphology," *Appl. Surf. Sci.*, vol. 616, no. -, pp. 1–9, Apr. 2023, doi: 10.1016/j.apsusc.2023.156470.

[43] C. Li, H. Jing, Z. Wu, and D. Jiang, "Layered Double Hydroxides for Photo(electro)catalytic Applications: A Mini Review," *Nanomaterials, MDPI*. Vol. 12, no. 3525, pp. 1-18, Oct. 01, 2022, doi: 10.3390/nano12193525.

[44] A. B. D. Nandiyanto, R. Zaen, and R. Oktiani, "Correlation between Crystallite Size and Photocatalytic Performance of Micrometer-Sized Monoclinic WO3 Particles," *Arabian Journal of Chemistry*, vol. 13, no. 1, pp. 1283–1296, Jan. 2020, doi: 10.1016/j.arabjc.2017.10.010.G. Eason, B. Noble, and I.N. Sneddon, "On certain integrals of Lipschitz-Hankel type involving products of Bessel functions," Phil. Trans. Roy. Soc. London, vol. A247, pp. 529-551, April 1955. (*references*)